Eclética Química Journal

Original article

revista.iq.unesp.br

| Vol. 47 | special issue 1 | 2022 |

Performance and stability of femtosecond laser-irradiated Fe_2O_3 materials as photocatalysts for methylene blue dye discoloration

Josiane Carneiro Souza[1+], Tiago Almeida Martins[1], Regiane Cristina de Oliveira[2], Julio Ricardo Sambrano[2], Cleber Renato Mendonça[3], Leonardo de Boni[3], Edson Roberto Leite[1], Elson Longo[1]

1. Federal University of São Carlos, Center for the Development of Functional Materials, São Carlos, Brazil.
2. São Paulo State University, Faculty of Science, Bauru, Brazil.
3. University of São Paulo, Institute of Physics, São Carlos, Brazil.

+Corresponding author: Josiane Carneiro Souza, **Phone:** +551633066600, **Email address:** josi3souza@gmail.com

ARTICLE INFO

Article history:
Received: July 04, 2021
Accepted: November 23, 2021
Published: April 11, 2022

Section Editors: Elson Longo and Juan Manuel Andrés Bort

Keywords:
1. defect density
2. polymorphism
3. dye
4. pollutant

ABSTRACT: The disposal of substances pollutant, such as methylene blue dye (MB), into wastewater, arouses the interest of technologies to remove these pollutants. The discoloration of MB by photocatalysis and using femtosecond laser-irradiated Fe_2O_3 materials as photocatalysts proved to be a promising way to treat this pollutant. Here, Fe_2O_3 obtained by the conventional hydrothermal process and heat-treatment, subsequently femtosecond laser-irradiated treatment. Materials obtained with a mixture of irradiated α-Fe_2O_3 and ε-Fe_2O_3 phases revealed lower crystallinity than irradiated α-Fe_2O_3 samples. The irradiation treatment and the increase in crystallinity were crucial to improve the performance of α-Fe_2O_3 irradiated sample in the discoloration of MB, which reached 90% in 75 min of dye solution exposure under UV irradiation. The irradiation treatment proved to allow greater exposure of the particle surfaces, which coalesced and presented a greater distribution of medium size, indicating a more heterogeneous morphology in the irradiated samples. As a result, there was an increase in active sites due to the density of defects generated, which facilitated the dye degradation process.

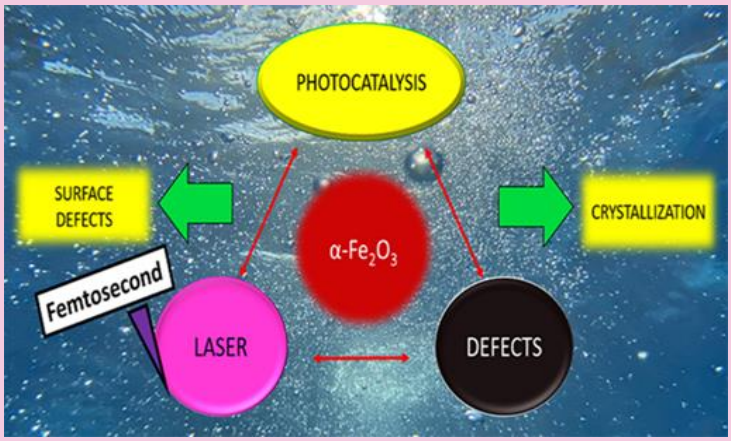

Eclética Química Journal, vol. 47, special issue 1, 2022, 105-119
ISSN: 1678-4618
DOI: 10.26850/1678-4618eqj.v47.1SI.2022.p105-119

1. Introduction

Hematite (α-Fe_2O_3) and ε-Fe_2O_3 are two of the five known iron oxide polymorphs which have different crystal structures under normal conditions of temperature and pressure (CNTP) (Machala *et al.*, 2011; Tuček *et al.*, 2015). Under the conditions of α-Fe_2O_3, the material is more thermodynamically stable and abundant within the polymorphs of Fe_2O_3 (Machala *et al.*, 2011; Sivula *et al.*, 2011). During the period of expansion of the past Inca α-Fe_2O_3 was found on the surface of magmatic rocks due to years of aerobic weathering processes (Gialanella *et al.*, 2010; Sepúlveda *et al.*, 2019), among its first uses as pigments in primitive ruptured paints in prehistoric eras (Marean *et al.*, 2007) and more recently as dyes (Carneiro *et al.*, 2018). α-Fe_2O_3 can be obtained by thermally induced structural transformations of other oxides (Gialanella *et al.*, 2010; Gonçalves *et al.*, 2011) and/or other Fe_2O_3 polymorphs (Darezereshki, 2011; Ding *et al.*, 2007; Zboril *et al.*, 2002), as well as from reactions between iron salts (II) and (III) (Lassoued *et al.*, 2017; Papynov *et al.*, 2018; Sivula *et al.*, 2010).

ε-Fe_2O_3 was discovered in 1934 by Forestier and Guiot-Guillain (1934), but only received the name ε-Fe_2O_3 29 years later by the researchers Schrader and Büttner (1963). Its structural characterization was performed for the first time in 1998 by Tronc *et al.* (1998) and in 2005 Kelm and Mader (2005), Sakurai *et al.* (2005) developed a model called refinement to interpret the X-ray crystal structure of ε-Fe_2O_3, obtained in coherence with some experimental data, such as lattice parameters and electron density maps (Shabalina *et al.*, 2018). The first thin films of ε-Fe_2O_3 were prepared in 2010 (Gich *et al.*, 2010); however, their chemical stability was determined eight years later at pressures up to 27 GPa (Sans *et al.*, 2018). ε-Fe_2O_3 is a metastable material between the polymorphs α-Fe_2O_3 and/or γ-Fe_2O_3 (Tronc *et al.*, 1998). Although it is found as biogenic nanoparticles mixed with magnetite and is present in some clays, this material is not very abundant in nature. Additionally, its particles have a low surface energy, which guarantees the formation and existence of ε-Fe_2O_3 (Gich *et al.*, 2007; McClean *et al.*, 2001; Petersen *et al.*, 1987).

Since α-Fe_2O_3 is an n-type semiconductor with a gap energy between 1.9 and 2.2 eV, it is considered as a potential sunlight converter, which uses solar energy to generate clean energy, such as electricity or green fuel (e.g., H_2) (Gratzel, 2001; Tamirat *et al.*, 2016). For such reason, it has been widely studied in photoelectrochemical processes (Sivula *et al.*, 2010; 2011; Trindade *et al.*, 2020). Fe_2O_3 materials can also be applied as carrier of drugs to treat cancer cells (Liong *et al.*, 2008; Mandriota *et al.*, 2019), lithium batteries (Gu *et al.*, 2013), gas sensors (Gou *et al.*, 2008), pigments (Carneiro *et al.*, 2018) and dyes (Ahmed *et al.*, 2013). Many studies have used Fe_2O_3 materials as photocatalysts or adsorbents in the degradation of dyes present in industrial effluents (paper, textiles, leather) especially methylene blue (MB), which is resistant to chemical and biological treatment and can produce more toxic substances than the dye itself during its chemical decomposition (Ahmed *et al.*, 2013; Crini, 2005; Sharma *et al.*, 2011).

The versatility of Fe_2O_3 materials is attributed to their distinct crystal structures, resulting in different physicochemical properties (Machala *et al.*, 2011; Sakurai *et al.*, 2009). What makes these materials versatile with interesting technological applications is the greater understanding of the association of their properties with their crystal structures, especially concerning the effects of structural order and disorder (Pottker *et al.*, 2018). It is known that the structural modification on the surface of particles irradiated using femtosecond laser technology improves the structural and ablation properties of the material (Keller, 2003; Sugioka and Cheng, 2014). Such modification can be assigned to the creation of cations and oxygen vacancies that modulate the electronic states in the valence band of the material (Assis *et al.*, 2020). This study evaluates the performance of thermally treated and femtosecond laser-irradiated Fe_2O_3 samples for the discoloration of methylene blue (MB) dye under UV irradiation.

2. Experimental

The Fe_2O_3 particles were obtained by the conventional hydrothermal process, according to a procedure similar to that reported by Gou *et al.* (2008): 2 mmol of $Fe(NO_3)_3{\cdot}9H_2O$, 4 mmol of trisodium citrate dihydrate and 5 mmol of urea were dissolved separately in 10 mL of deionized water and subsequently dissolved and placed in a hydrothermal reactor under constant stirring. The hydrothermal process was carried out at 160 °C for 10 h. After cooling, the precipitates were washed with deionized water and alcohol, and then dried at 90 °C for 6 h. Lastly, they were heat-treated at 860 and 900 °C for 30 min.

Fe_2O_3 samples were irradiated by a Ti:Sapphire laser (CPA-2001 system from Clark-MXR Inc.), at 775 nm, 150 fs (FWHM) and a repetition rate of 1 Hz. The samples were irradiated with an average power of 300 mW and positioned within the Rayleigh range. The

Eclética Química Journal, vol. 47, special issue 1, 2022, 105-119
ISSN: 1678-4618
DOI: 10.26850/1678-4618eqj.v47.1SI.2022.p105-119

experiment was carried out following Assis *et al.* (2020). The nonirradiated samples were named hematite+epsilon-Fe2O3 (EPHE) and hematite-Fe2O3 (HE). After irradiation, they were denominated EPHEI and HEI, respectively.

The thermal behavior of Fe_2O_3 particles obtained by the hydrothermal process were evaluated by thermogravimetry (TGA) and differential thermal analysis (DTA), and then heated up to 1300 °C in an O_2 atmosphere with a flow of 50 mL min^{-1} (NETZSCH - Cell 409).

The structural characterization of Fe_2O_3 samples was performed by X-ray diffraction (XRD), Raman spectroscopy and scanning electron microscopy (SEM). For the XRD measurements, a diffractometer (Shimadzu) with Cu Kα radiation (λ = 1.5406 Å) was used, and the XRD patterns were acquired with steps of 0.02° and an angular range of 10 to 110°. The data obtained were analyzed using the Rietveld (1969) method with the aid of the general structure analysis system (GSAS) software (Von Dreele and Larson, 1994). Raman spectra were obtained in the range of 100–1000 cm^{-1} using a Senterra spectrometer (Bruker) coupled to a 785 nm He–Ne laser excitation source with a power of 1 mW and a microscope with a 20× objective.

The morphology of the Fe_2O_3 samples was analyzed through images obtained in a Zeiss – Supra 35 scanning electron microscope. The images were obtained by secondary electron detection (ETD, Everhart – Thornley detector) with a 10 kV incident beam. Transmission electron microscopy (TEM) images were captured in high resolution (HRTEM) using an FEI – Tecnai F20 microscope operating in the brightfield. One μm-scale scanning electron micrographs were used to construct the frequency histogram and the mean size modal distribution curve versus particle size. The count of 150 particles was inspected and the measurements were performed by the ImageJ software (Schneider *et al.*, 2012) using the linear method.

The UV-Vis spectra were obtained over a range of 800–300 nm in diffuse reflectance mode at room temperature using a Varian Cary 5G spectrometer.

The photocatalytic activity of nonirradiated and irradiated Fe_2O_3 samples was tested for the discoloration of the methylene blue dye (MB; $[C_{16}H_{18}ClN_3S]$; 99.5% purity, Mallinckrodt) in relation to the exposure time under UV irradiation. The loss of MB coloration was observed by aliquots of Fe_2O_3 materials dispersed in the dye solution under UV radiation at different collection times. The concentration of the aqueous solution of MB used in the photocatalysis experiments was provided by a calibration curve. The maximum absorbance ($\lambda_{maximum}$) measurement of MB was performed using a UV-Vis spectrometer (V-660 Jasco). As the dye follows Beer's Law (Grasse *et al.*, 2016), the calibration curve provided the aqueous concentration of the MB index in the photocatalytic study of nonirradiated and irradiated Fe_2O_3 materials.

The experiments were carried out by dispersing 50 mg of the sample in 50 mL of MB solution in an ultrasound bath inside an open reactor with a controlled temperature of 20 °C and water circulation. The sample-dye adsorption process was performed by stirring this dispersion in the dark for 30 min. The photocatalytic system was obtained by illuminating this dispersion with six UV lamps (TUV Philips, 15 W with maximum intensity of 254 nm). Aliquots were removed at time zero and other predetermined times (5, 10, 20, 30, 45, 60 and 75 min), the absorbance changes were measured by a spectrophotometer (V-660 Jasco), while the photocatalytic stability of the sample with the best performance was obtained from the recycling test results.

3. Results and discussion

There are four thermal events according to the TGA and differential thermal DTA curves of the Fe_2O_3 sample obtained by the conventional hydrothermal process, as showed in Fig. 1. The TGA curve demonstrates that the thermal stability of the sample occurred at 500 °C. The processes with energy absorption were identified at 110 °C, which corresponds to the sample dehydration, and at 650 °C, indicating that above this temperature hematite presents paramagnetic behavior (Liu *et al.*, 1997). At 243 and 860 °C, two exothermic events were observed, the first due to the release of gases and organic impurities from the process of particle obtention, and the second attributed to the ε-Fe_2O_3 → α-Fe_2O_3 phase transition (Dézsi and Coey, 1973). From this result, it was possible to perform the heat-treatment of the Fe_2O_3 samples.

The vibrational modes of Raman showing EPHE and EPHEI were identified as shown in Fig. 2. The vibrational modes of single-phase ε-Fe_2O_3 samples phase are not identified in the literature yet. The determination of the wavenumbers referring to the ε-Fe_2O_3 phase was performed from a Lorentzian fit of the Raman scattering spectrum bands. Thus, it was possible to distinguish the vibrational modes of the ε-Fe_2O_3 and α-Fe_2O_3 phases (López-Sánchez *et al.*, 2016). The vibrational modes agree with the

Eclética Química Journal, vol. 47, special issue 1, 2022, 105-119
ISSN: 1678-4618
DOI: 10.26850/1678-4618eqj.v47.1SI.2022.p105-119

vibrational modes reported by López-Sánchez *et al.* (2016), the ε-Fe_2O_3 phase has 117 active Raman vibrational modes: $29A_1 + 30A_2 + 29B_1 + 29B_2$, considering that the same has space group Pna21. Sample EPHE (Fig. 2a) showed nine active modes of the ε-Fe_2O_3 phase in wavenumbers in the range 120 to 600 cm^{-1}.

According to the literature (Faria *et al.*, 1997), α-Fe_2O_3 exhibits seven modes of active phonons ($2A_{1g} + 5E_g$) allowed in Raman. Sample EPHE shows two modes in 226 and 496 cm^{-1}, attributed to A_{1g}, and others in 245, 293, 410 and 610 cm^{-1}, assigned to E_g.

The changes observed in the Raman vibrational modes of the irradiated samples (Fig. 2b) are a consequence of the irradiation treatment, which provided an increase in the structural disorder within the crystal lattice of samples EPHEI and HEI. Compared to the nonirradiated samples, the high full-width at half-maximum (FWHM) values of the Raman bands, and the absence of active vibrational modes of the irradiated samples (Tab. 1) indicated that the irradiation treatment caused a distortion in the crystal lattice of the samples and an increase in the defect density, leading to the breaking of Fe–O bonds. These results contribute to changes in the physicochemical properties of the irradiated samples.

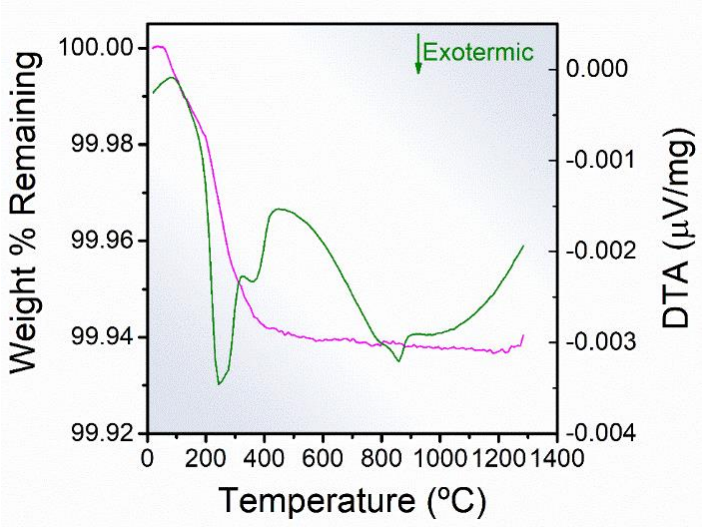

Figure 1. Differential thermal curve (olive line) and TGA curve (magenta line) of Fe_2O_3 sample obtained by the conventional hydrothermal process.

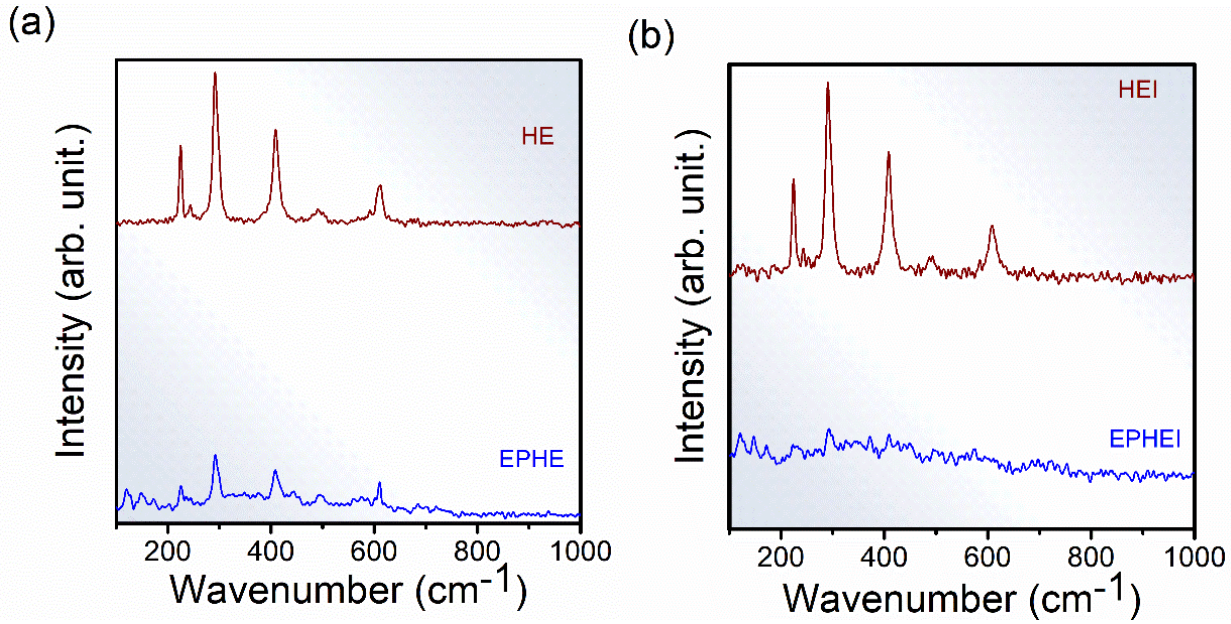

Figure 2. Raman spectra for **(a)** nonirradiated samples and **(b)** irradiated samples.

X-ray diffraction patterns of samples EPHE and EPHEI (Fig. 3) presented peaks indexed to the inorganic crystal structure database (ICSD) number 415250 (Kelm and Mader, 2005; Sakurai *et al.*, 2005) and 15840 (Blake *et al.*, 1966), and corresponding to ε-Fe_2O_3 to α-Fe_2O_3 phases, respectively, characterizing these materials as multiphase. These phases have an orthorhombic (Pna 21) and rhombohedral (R-3cH) structure with eight and six molecular formulas per unit cell (Z = 8 and 6), respectively. On the other hand, samples HE and HEI are formed by α-Fe_2O_3 and are considered monophasic. This preferential formation is due to the increase in temperature to 900 °C during the heat-treatment when compared to samples EPHE and EPHEI.

Eclética Química Journal, vol. 47, special issue 1, 2022, 105-119
ISSN: 1678-4618
DOI: 10.26850/1678-4618eqj.v47.1SI.2022.p105-119

Table 1. Wavenumbers (cm $^{-1}$) and full widths at half maximum (FWHM) for nonirradiated and irradiated samples.

Wavenumber (cm^{-1}) EPHE	FWHM (cm^{-1}) EPHE	Wavenumber (cm^{-1}) EPHEI	FWHM (cm^{-1}) EPHEI	Wavenumber (cm^{-1}) HE	FWHM (cm^{-1}) HE	Wavenumber (cm^{-1}) HEI	FWHM (cm^{-1}) HEI
123.4 ± 0.1	11.3	122.7 ± 0.3	13.8	-	-	-	-
147.9 ± 0.2	9.6	148.2 ± 0.2	13.3	-	-	-	-
172.1 ± 0.3	10.5	172.0 ± 0.3	11.1	-	-	-	-
226.1 ± 0.3	6.8	225.7 ± 0.3	2.8	225.8 ± 0.1	8.9	224.9 ± 0.1	8.7
244.9 ± 0.2	6.2	-	-	244.1 ± 0.2	11.5	245 ± 2	45.0
293.8 ± 0.2	13.8	293.9 ± 0.3	4.9	292.8 ± 0.1	14.7	292.1 ± 0.1	15.7
326.7 ± 0.3	7.1	325.4 ± 0.2	6.0	-	-	-	-
349.6 ± 0.2	6.2	350.6 ± 0.1	4.7	-	-	-	-
375.5 ± 0.2	12.2	373.9 ± 0.1	5.1	-	-	-	-
409.1 ± 0.3	16.6	409.3 ± 0.3	6.9	409.3 ± 0.1	15.6	408.9 ± 0.1	19.0
443.0 ± 0.3	8.4	-	-	-	-	-	-
560.9 ± 0.2	7.8	-	-	-	-	-	-
590.0 ± 0.2	6.7	-	-	-	-	-	-
495.3 ± 0.3	32.5	494.3 ± 0.2	10.4	494.0 ± 2.1	25.2	493.0 ± 0.3	22.3
610.1 ± 0.2	9.9	-	-	610.5 ± 0.2	12.2	608.7 ± 0.1	19.1

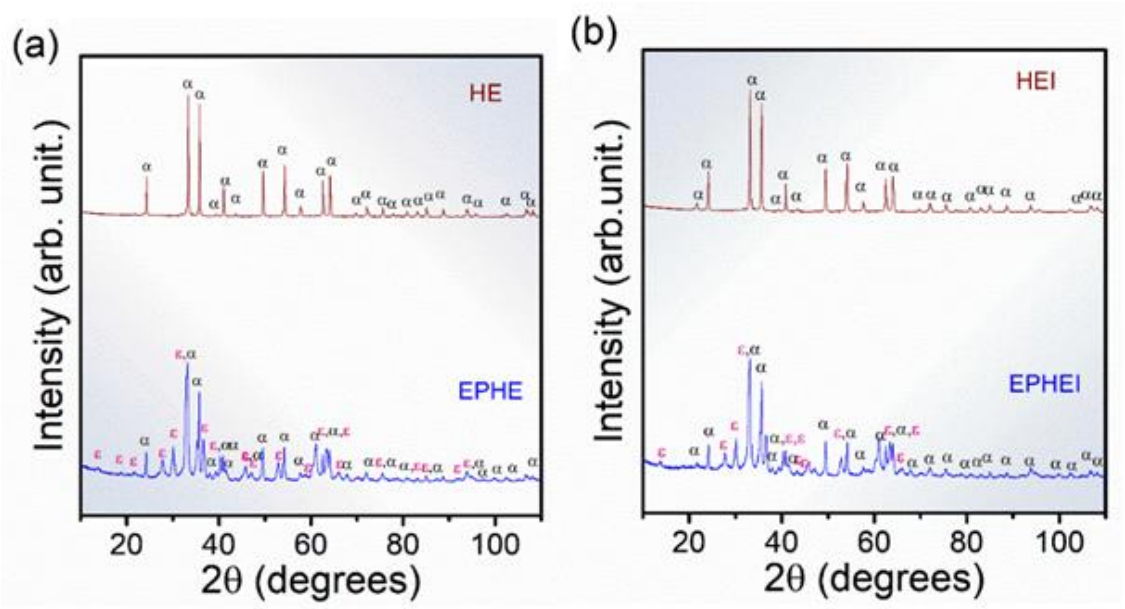

Figure 3. X-ray diffraction patterns for the ε-Fe_2O_3 and α-Fe_2O_3 of the samples heat-treated at 860 and 900 °C for 30 min. In **(a)** nonirradiated samples and **(b)** irradiated samples.

The results of structural refinement by the Rietveld (1969) method are shown in Tab. 2 and Fig. 4. Table 2 presents the lattice parameters and the percentage of phases of the samples before and after the irradiation treatment, whereas Fig. 4 shows typical Rietveld refinement graphs. It is possible to observe that the diffraction patterns calculated and obtained in Fig. 3 are related to high structural order or long-range and well-defined peaks.

The results of two lattice parameters presented in Tab. 2 are consistent with the previous studies of α-Fe_2O_3 and ε-Fe_2O_3 phases (Blake *et al.*, 1966; Kelm and Mader, 2005; Sakurai *et al.*, 2005). In this study, EPHE and EPHEI showed 62% of the ε-Fe_2O_3 phase, while HE exhibited crystallized α-Fe_2O_3 as the preferential phase, which is indicative of the increase in temperature without heat-treatment. These results refer to the nonlinearity of the adjustment parameter (Rw %) for different processes of crystallization, solubilization and recrystallization. Microstrain results from irradiated samples (EPHEI and HEI) revealed higher values than those shown by nonirradiated samples (EPHE and HE), demonstrating that the irradiation treatment favored or increased the density of defects and stress in the crystalline lattice of the materials.

Eclética Química Journal, vol. 47, special issue 1, 2022, 105-119
ISSN: 1678-4618
DOI: 10.26850/1678-4618eqj.v47.1SI.2022.p105-119

Table 2. Parameters obtained from Rietveld refinements of Fe_2O_3 samples.

Sample			EPHE	EPHEI	HE	HEI	ε-Fe_2O_3*	α-Fe_2O_3**
α-Fe_2O_3	Lattice parameters (Å)	a = b	5.035	5.037	5.040	5.035	-	5.038
		c	13.733	13.738	13.758	13.748	-	13.772
	V (Å^3)		301.50	301.93	302.70	301.89	-	302.72
	Crystallite size (Å)		0.45	0.40	0.84	0.73	-	-
	Microstrain		1282.7	2215.5	921.9	1390.9	-	-
	% Wt fraction		0.376	0.379	1.000	1.000	-	
ε-Fe_2O_3	Lattice parameters (Å)	a	5.091	5.091	-	-	5.071	-
		b	8.781	8.789	-	-	8.736	-
		c	9.465	9.470	-	-	9.418	-
	V (Å^3)		423.09	423.74	-	-	417.25	-
	Crystallite size (Å)		0.25	0.25	-	-	-	-
	Microstrain		–599.4	–1741.8	-	-	-	
	% Wt fraction		0.624	0.621	-	-	-	-
Rw%			9.414	8.943	-	-	-	-

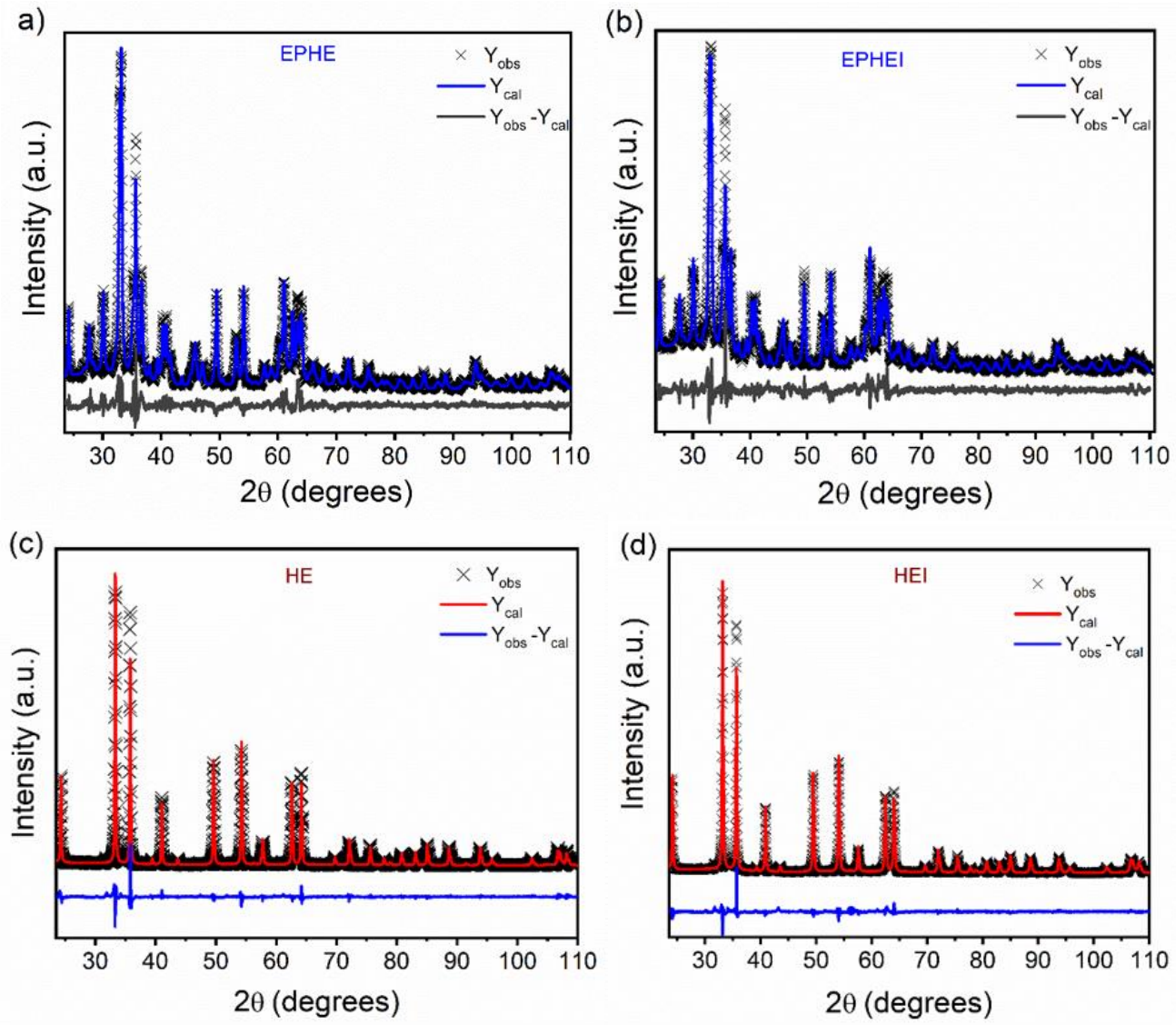

Figure 4. Rietveld refinement plot of nonirradiated in **(a, c)** and **(b, d)** irradiated samples.

Eclética Química Journal, vol. 47, special issue 1, 2022, 105-119
ISSN: 1678-4618
DOI: 10.26850/1678-4618eqj.v47.1SI.2022.p105-119

Figure 5 illustrates the UV-Vis spectra in diffuse reflectance mode in the 250–800 nm range for the nonirradiated and irradiated samples. The absorbance close to the 570 nm region shows that these samples have application as absorbers (Sarma *et al.*, 2020).

The calculations performed to determine the energy of the samples in the forbidden band (E_{gap}) were obtained according to Wood and Tauc (1972) and Chen *et al.* (2013). The indirect transitions of the samples resulted in E_{gap} values consistent with the literature (Pandey *et al.*, 2014). Compared to the nonirradiated samples, EPHEI and HEI showed a reduction in their E_{gap} value, indicating that the irradiation treatment caused the samples to present a more conductive behavior with greater structural disorder at medium-range (Pinatti *et al.*, 2020). It can be attributed to the presence of electronic levels within the forbidden band, which are associated with crystalline lattice disturbances. These results corroborate those obtained in the Raman and XRD analyses.

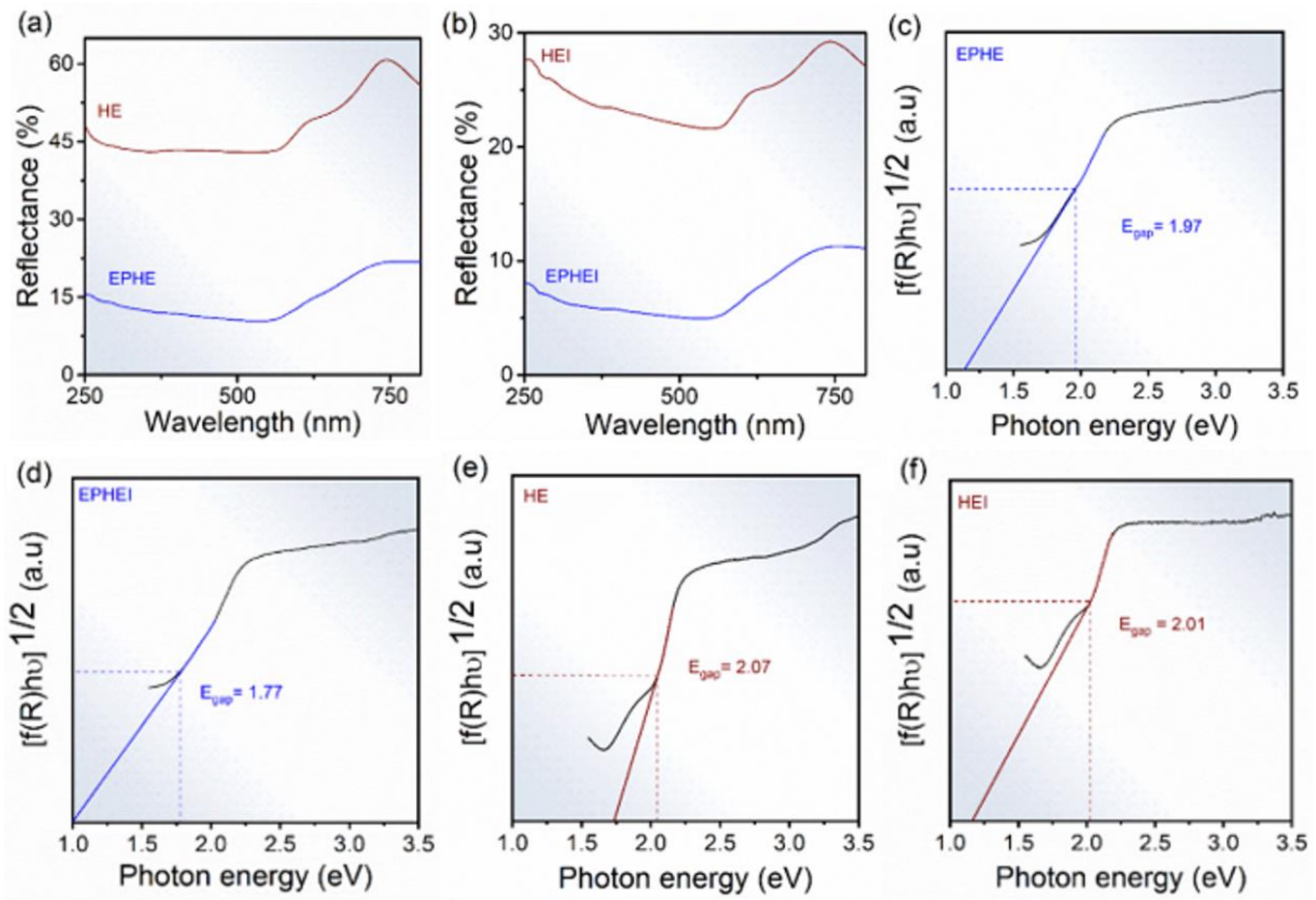

Figure 5. UV-Vis spectra in **(a, b)** and energy gap. In **(c, e)** nonirradiated samples and **(d, f)** irradiated samples.

The electron micrographs in Fig. 6 reveal that sample EPHE has a heterogeneous morphology with clusters in the shape of irregular plates and equiaxed structures on the plates. In turn, HE showed that the α-Fe_2O_3 particles have a homogeneous morphology with clusters of irregular plaques. The same change was observed in EPHEI and HEI, even though the irradiation treatment allowed the formation of equiaxed particles on the agglomerated structures, including, in some regions of the samples, the phenomenon of coalescence resulting from diffusion processes of matter during irradiation (Anastasiou *et al.*, 2016).

Eclética Química Journal, vol. 47, special issue 1, 2022, 105-119
ISSN: 1678-4618
DOI: 10.26850/1678-4618eqj.v47.1SI.2022.p105-119

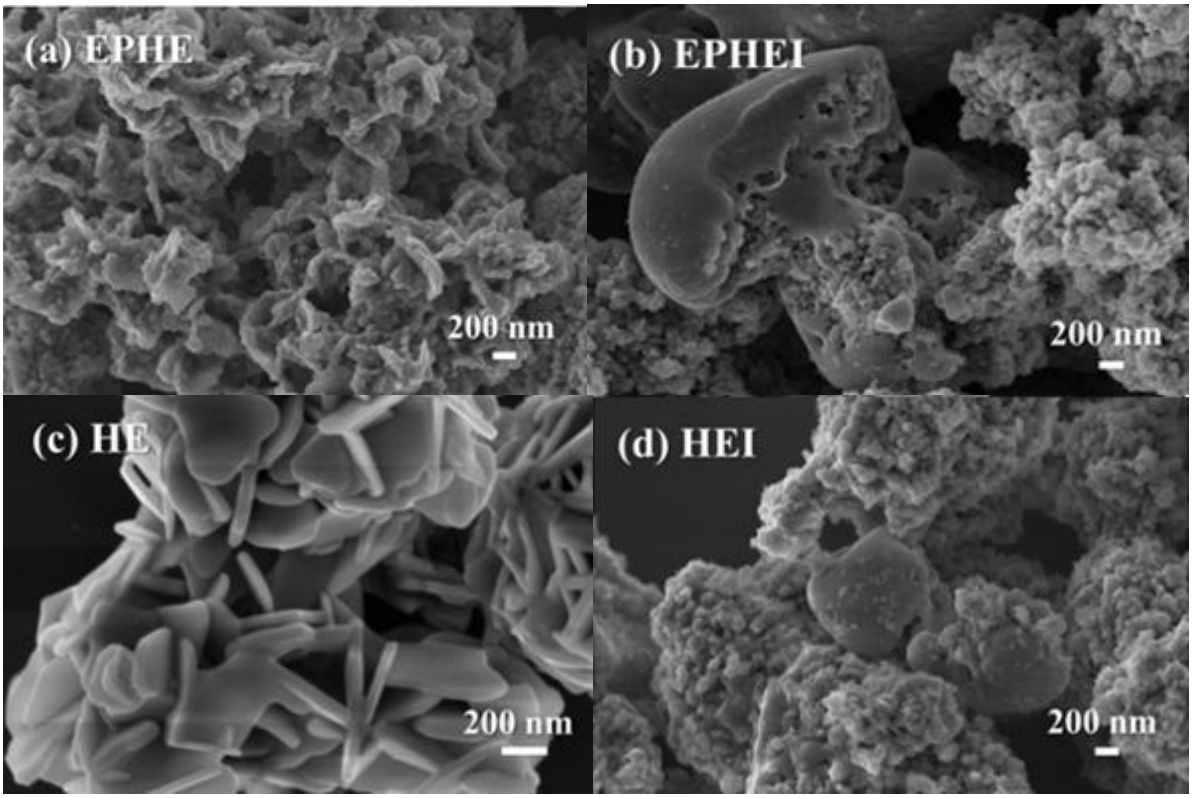

Figure 6. Micrographs of the nonirradiated in **(a, c)** and **(b, d)** irradiated samples.

The frequency histograms in Fig. 7 reveal an average size of 41 and 40 nm for the particles of samples EPHE and HE, respectively, and 49 and 54 nm for the irradiated samples EPHEI and HEI, respectively. It can be noted that the mean size distribution curve of the EPHE and EPHEI particles was very similar to each other. On the other hand, the mean size distribution curve of HEI became much broader than that of HE, indicating that there was an increase in the morphological heterogeneity.

Images obtained from high-resolution micrographs (HRTEM) of the nonirradiated and irradiated samples are displayed in Fig. 8. The crystallinity of the samples made it possible to obtain the indexation of the Fe_2O_3 phases. The insets show that the nonirradiated and irradiated samples crystallized in the ε-Fe_2O_3 and α-Fe_2O_3 phases, corroborating the results of the Raman spectra and XDR patterns. The irradiation treatment increased the defect density and avoided the ε-Fe_2O_3 to α-Fe_2O_3 phase transition in sample EPHEI.

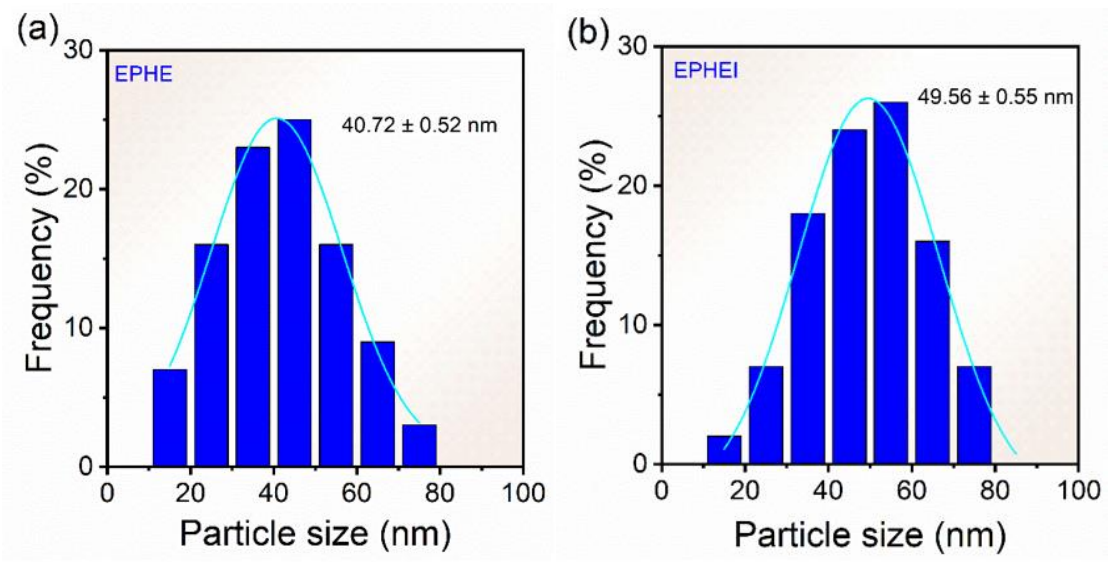

Eclética Química Journal, vol. 47, special issue 1, 2022, 105-119
ISSN: 1678-4618
DOI: 10.26850/1678-4618eqj.v47.1SI.2022.p105-119

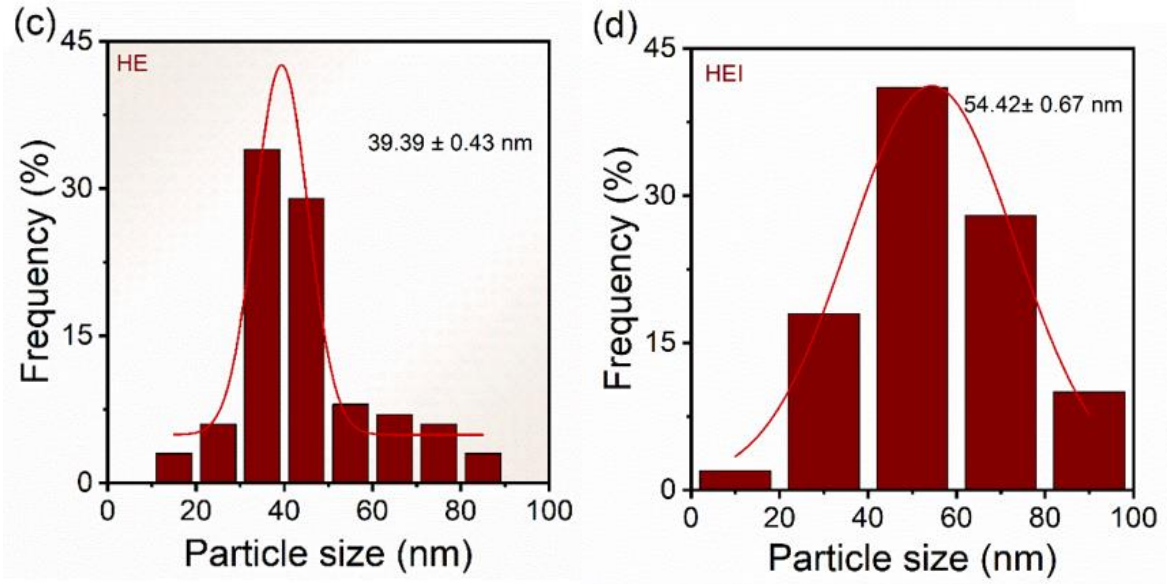

Figure 7. Frequency histograms of the nonirradiated in **(a, c)** and **(b, d)** irradiated samples.

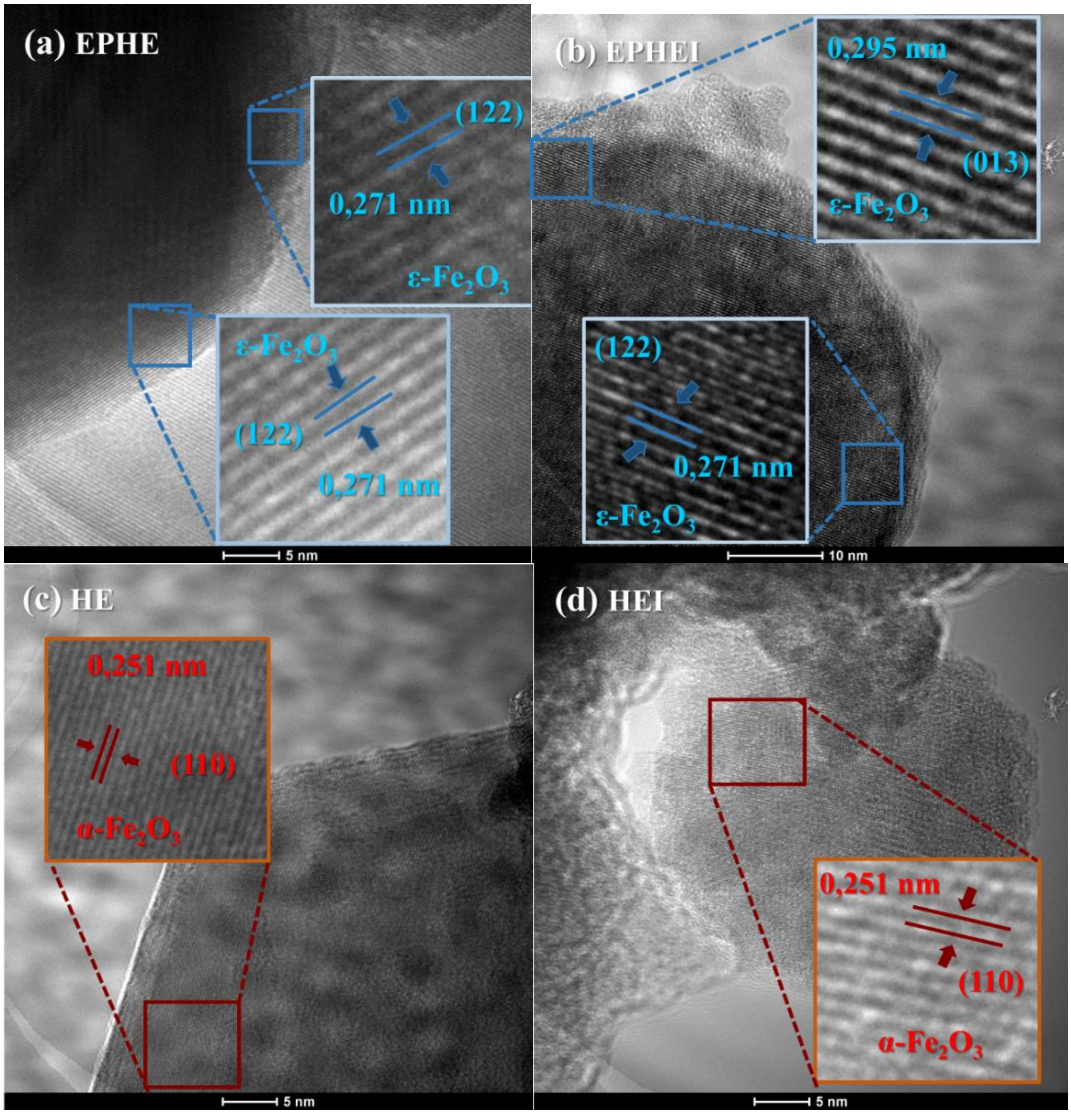

Figure 8. Transmission electron microscopy imagens of the nonirradiated in **(a, c)** and **(b, d)** irradiated samples.

Eclética Química Journal, vol. 47, special issue 1, 2022, 105-119
ISSN: 1678-4618
DOI: 10.26850/1678-4618eqj.v47.1SI.2022.p105-119

The MB calibration curve (Fig. 9) was constructed from the solutions of the standard MB at pH = 7. The concentration of aqueous solutions of MB was estimated by measuring the absorbance at maximum wavelengths of MB ($\lambda_{maximum}$= 668 nm) (Sheng and Mat Yunus, 2005). The adjustment of the experimental data was given by a straight line with a regression coefficient of R^2 = 0.9990. The calibration curve allowed us to determine that the concentration of 52.33 mg L^{-1} of MB had a maximum absorbance value of 1.0067, which is in agreement with the value found by Al-Rubayee *et al.* (2016). This was the concentration used in the photocatalysis test.

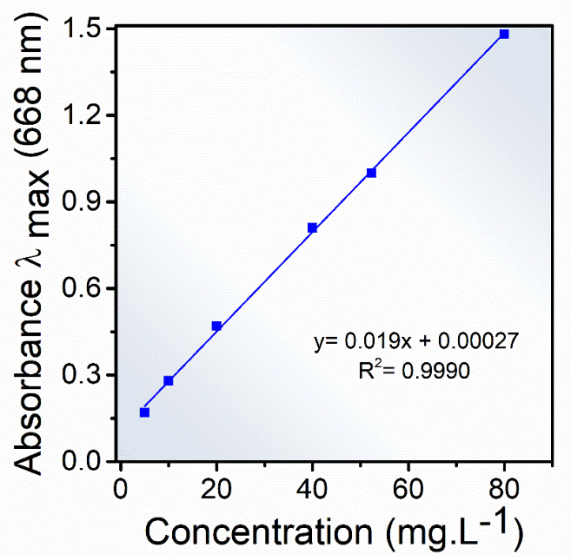

Figure 9. Calibration curve methylene blue at different concentrations 5–80 mg.L^{-1}.

The photocatalytic activity of nonirradiated and irradiated Fe_2O_3 samples was compared when MB was subjected to UV irradiation, in the absence of photocatalysts and under the same experimental conditions. Figure 10a shows the relationship among the equilibrium adsorption concentration, the concentration after irradiation (C_N/C_0) and the irradiation time. The MB sample without catalyst showed much lower discoloration than catalyzed samples. The discoloration of MB in 75 min photocatalyzed by HEI was 90%. However, HE showed a similar discoloration profile in the absence of a catalyst. In relation to the dye adsorption, samples EPHE and EPHEI reached values of 60 and 35% in the dark, respectively. In contrast, HE (α-Fe_2O_3) adsorbed 20% of the dye within 30 min of exposure in the dark. Allawi *et al.* (2020) studied the adsorption process of 100 mg of α-Fe_2O_3 catalyst in a 20 mg L^{-1} MB solution at pH 7.6. They observed that in 6 min of exposure in the dark, the dye adsorption was ~10 %. Considering the results achieved by samples EPHE and EPHEI, it is possible to then infer that the presence of the ε-Fe_2O_3 phase significantly influenced the MB adsorption process. During the photocatalysis of EPHE and EPHEI, the discoloration was 8 and 15%, respectively, which is in accordance with the results obtained by Ahmed *et al.* (2013). These findings show that samples EPHE and EPHEI behave as MB adsorbent materials, being promising for MB photocatalysis. Regarding the photocatalytic activity of HEI, the recycling test was performed following the procedure described Trench *et al.* (2018). The effect of photocatalytic activity of each cycle is shown in Fig. 10c. It is possible to observe that the photocatalytic activity of this sample decreased over the cycles, which can be attributed to the loss of material due to washing processes for dye removal. On the other hand, such sample (HEI) showed good stability as a photocatalyst.

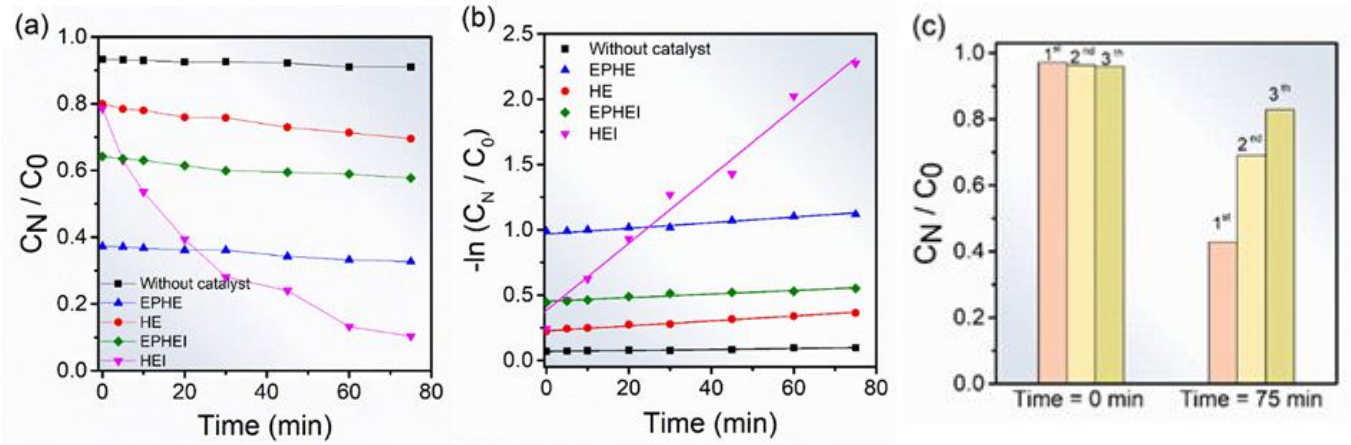

Figure 10. Photocatalytic discoloration of MB (52.33 mg L^{-1}). In **(a)** without catalyst and Fe_2O_3 nonirradiated and irradiated materials and **(b)** Determination of the rate constant by log plot and **(c)** Recycle test of HEI sample.

Eclética Química Journal, vol. 47, special issue 1, 2022, 105-119
ISSN: 1678-4618
DOI: 10.26850/1678-4618eqj.v47.1SI.2022.p105-119

For the MB dye, the solution concentration was considered very low. In order to quantitatively compare the obtained results, a kinetic study was carried out using a pseudo first-order reaction from the Langmuir–Hinshelwood model, as showed Eq. 1 (Guettaï and Amar, 2005):

$$k't = -\ln\left(\frac{C_N}{C_0}\right) \quad (1)$$

where k' and t represent the constant reaction rate and the irradiation time, respectively. Figure 10b shows the kinetic behavior of MB discoloration. The reaction constants found were 2.67×10^{-2}, 1.39×10^{-3}, 1.80×10^{-3}, 1.87×10^{-3}, 3.52×10^{-4} min^{-1} for HEI, EPHEI, HE, EPHE and the sample without catalyst, respectively. In comparison with the sample without catalyst, EPHE, EPHEI and HE showed an increase in the reaction speed in one order of magnitude, while HEI exhibited a constant speed with two orders of magnitude.

Figures 6 and 8 illustrate the morphology of the nonirradiated samples (EPHE and HE) under thermal treatment. It could be observed that the femtosecond laser-irradiation treatment led to the formation of different morphologies in EPHEI and HEI that interfere with the absorption and electron transfer processes, presenting different photocatalytic activities (Vu *et al.*, 2019). The lower photocatalytic activity was due to the reduction of active reaction sites in the studied samples (Huang *et al.*, 2015). The irradiation treatment directly affected the surface of the particles, causing an increase in the density of surface defects, thus improving the photocatalytic properties of these samples.

This result is very significant compared to the development of α-Fe_2O_3 materials as a photocatalyst for MB discoloration at room temperature, which reached a value of 78% in 6 h of UV irradiation (Vu *et al.*, 2019). In fact, the irradiation treatment proved to be very efficient to improve the photocatalytic activity of sample HEI, composed solely of α-Fe_2O_3. This improvement was also attributed to the defects generated on the surface of the particles (Vu *et al.*, 2019).

The α-Fe_2O_3 present in the studied samples has short diffusion length of the minority carriers (holes) (Wheeler *et al.*, 2012) and low conductivity of the majority carriers (electrons) (Kennedy and Frese Junior, 1978), resulting in difficulty in separating the photogenerated electron-hole pairs, and consequently influencing the photocatalytic activity results of these materials. On the other hand, ε-Fe_2O_3 is a material difficult to be obtained in isolation (Danno *et al.*, 2013; Dézsi and Coey, 1973; Shanenkov *et al.*, 2019; Wang *et al.*, 2019). For such reason, its attention is more focused on its interesting magnetic properties, as the anisotropic particles in this material can lead to the formation of a single magnetic domain, generating a large coercive field compared to other Fe_2O_3 polymorphs, and thus having advanced magnetic applications (Jin *et al.*, 2004; Machala *et al.*, 2011). However, in this study it was very interesting to investigate the photocatalytic properties of this material against α-Fe_2O_3.

Since the photocatalytic process of HEI occurred by the transfer of surface charge, there was a consequent increase in defect density (Huang *et al.*, 2015). Such sample absorbed energy of the photon generated by UV irradiation to form charge carriers (electron-hole pairs) that participate in the photooxidation on the sample surface. Minority carriers form very reactive hydroxy radicals (·OH), which are the main active species used to decolor MB (Zhao *et al.*, 2004). In contrast, majority carriers captured by dissolved oxygen in the MB solution form superoxide radicals anions ($\cdot O_2^-$) and/or peroxide radicals, which have the ability to break down MB molecules until mineralizing them into CO_2 and H_2O (Vadivel *et al.*, 2014). In turn, $\cdot O_2^-$ reacts with minority carriers of the sample, forming peroxides and releasing oxygen and/or active OH radicals and peroxides, partially contributing to the degradation of MB (Huang *et al.*, 2015).

4. Conclusions

The optical properties of femtosecond laser-irradiated α-Fe_2O_3 materials showed a reduction in their band gap energy values and exhibited a more conductive behavior than nonirradiated samples due to the presence of electronic levels within the band gap range generated by the resulting defect density caused by irradiation.

According to the XRD patterns, the structural characterization showed that the high crystallinity of samples HE compared to EPHE influenced the increase in their photocatalytic activity due to the presence of the ε-Fe_2O_3 phase. On the other hand, the femtosecond laser irradiation treatment improved the photocatalytic properties of EPHEI compared to the nonirradiated sample (EPHE). A significant reduction in the Raman modes was observed for irradiated samples, indicating that their structural disorder at medium range was a result from the increase in the density of defects generated on the surface of their particles. Therefore, it was proven that sample HEI presented the best photocatalytic property, which was attributed to the

Eclética Química Journal, vol. 47, special issue 1, 2022, 105-119
ISSN: 1678-4618
DOI: 10.26850/1678-4618eqj.v47.1SI.2022.p105-119

synergistic effect of the high crystallinity of the α-Fe_2O_3 phase and the generation of defects caused by the irradiation treatment.

The morphological aspect of the samples revealed agglomerated particles that impaired the improvement of the photocatalytic properties of the samples. Therefore, samples EPHE, HE and EPHEI behaved as adsorbent materials for MB discoloration. These materials have the potential to be used together with photocatalysts to enhance MB degradation in a short period of dye exposure. The mean particle size distribution curve of HEI was wider than that of HE, indicating an increase in the morphological heterogeneity of the irradiated sample, which consequently favored the increase in its catalytic activity. The phase indexing in the HRTEM images showed that the irradiation treatment was not energetically favorable to the transformation of ε-Fe_2O_3 to α-Fe_2O_3, but sufficiently effective for the generation of surface defects in the particles of the irradiated samples (HEI and EPHEI).

Authors' contribution

Conceptualization: Souza, J. C.; Martins, T. A.; Oliveira, R. C.; Sambrano, J. R.; Boni, L.; Mendonça, C. R.; Leite, E. R.; Longo, E.
Data curation: Not applicable.
Formal Analysis: Souza, J. C.; Martins, T. A.; Oliveira, R. C.; Boni, L.
Funding acquisition: Mendonça, C. R.; Leite, E. R.; Longo, E.
Investigation: Souza, J. C.; Martins, T. A.; Oliveira, R. C.; Sambrano, J. R.
Methodology: Souza, J. C.; Martins, T. A.; Boni, L.
Project administration: Leite, E. R.; Longo, E.
Resources: Souza, J. C.; Martins, T. A.; Oliveira, R. C.; Boni, L.; Mendonça, C. R.; Leite, E. R.; Longo, E.
Software: Not applicable
Supervision: Longo, E.
Validation: Souza, J. C.; Martins, T. A.; Oliveira, R. C.; Sambrano, J. R Mendonça, C. R.; Boni, L.
Visualization: Souza, J. C.; Martins, T. A.; Oliveira, R. C.; Sambrano, J. R Mendonça, C. R.; Boni, L.
Writing – original draft: Souza, J. C.; Martins, T. A.; Oliveira, R. C.; Sambrano, J. R.; Boni, L.; Mendonça, C. R.; Leite, E. R.; Longo, E.
Writing – review & editing: Souza, J. C.; Martins, T. A.; Oliveira, R. C.; Sambrano, J. R.; Boni, L.; Mendonça, C. R.; Leite, E. R.; Longo, E.

Data availability statement

All data sets were generated or analyzed in the current study

Funding

Coordenação de Aperfeiçoamento de Pessoal de Nível Superior (CAPES). Finance Code: 001.

Fundação de Amparo à Pesquisa do Estado de São Paulo (FAPESP). Grant No: 2013/07296-2; 2019-08928-9; 2018/11283-7; 2021/01651-1.

Conselho Nacional de Desenvolvimento Científico e Tecnológico (CNPq). Grant No: 2019/88887.469176.

Acknowledgments

Not applicable.

References

Ahmed, M. A.; El-Katori, E. E.; Gharni, Z. H. Photocatalytic degradation of methylene blue dye using Fe_2O_3/TiO_2 nanoparticles prepared by sol–gel method. *J. Alloys Compd.* **2013**, *553*, 19–29. https://doi.org/10.1016/j.jallcom.2012.10.038

Allawi, F.; Juda, A. M.; Radhi, S. W. Photocatalytic degradation of methylene blue over MgO/α-Fe2O3 nano composite prepared by a hydrothermal method. *AIP Conf. Proc.* **2020**, *2290* (1), 030020. https://doi.org/10.1063/5.0029461

Al-Rubayee, W. T.; Abdul-Rasheed, O. F.; Ali, N. M. Preparation of a Modified Nanoalumina Sorbent for the Removal of Alizarin Yellow R and Methylene Blue Dyes from Aqueous Solutions. *J. Chem.* **2016**, *2016*, 4683859. https://doi.org/10.1155/2016/4683859

Anastasiou, A. D.; Thomson, C. L.; Hussain, S. A.; Edwards, T. J.; Strafford, S.; Malinowski, M.; Mathieson, R.; Brown, C. T. A.; Brown, A. P.; Duggal, M. S.; Jha, A. Sintering of Calcium Phosphates with a Femtosecond Pulsed Laser for Hard Tissue Engineering. *Mater. Des.* **2016**, *101*, 346–354. https://doi.org/10.1016/j.matdes.2016.03.159

Assis, M.; Ribeiro, R. A. P.; Carvalho, M. H.; Teixeira, M. M.; Gobato, Y. G.; Prando, G. A.; Mendonça. C. R.; Boni, L.; Oliveira, J. A. de; Bettini, J.; Andrés, J.; Longo, E. Unconventional Magnetization Generated from Electron Beam and Femtosecond Irradiation on α-Ag2WO4: A Quantum Chemical Investigation. *ACS Omega.* **2020**, *5*, 10052–10067. https://doi.org/10.1021/acsomega.0c00542

Blake, R. L.; Hessevick, R. E.; Zoltai, T.; Finger, L. W. Refinement of the hematite structure. *Am. Mineral.* **1966**, *51* (1–2), 123–129.

Carneiro, J.; Tobaldi, D. M.; Hajjaji, W.; Capela, M. N.; Novais, R. M.; Seabra, M. P.; Labrincha, J. A. Red mud as a substitute coloring agent for the hematite pigment. *Ceram. Int.* **2018**, *44* (4), 4211–4219. https://doi.org/10.1016/j.ceramint.2017.11.225

Chen, Z.; Miller, E.; Dinh, H. N. *Photoelectrochemical Water Splitting*: Standards, Experimental Methods, and Protocols. Springer, 2013. https://doi.org/10.1007/978-1-4614-8298-7

Crini, G. Recent developments in polysaccharide-based materials used as adsorbents in wastewater treatment. *Prog. Polym. Sci.* **2005**, *30* (1), 38–70. https://doi.org/10.1016/j.progpolymsci.2004.11.002

Danno, T.; Nakatsuka, D.; Kusano, Y.; Asaoka, H.; Nakanishi, M.; Fujii, T.; Ikeda, Y.; Takada, J. Crystal Structure of β-Fe_2O_3 and Topotactic Phase Transformation to α-Fe_2O_3. *Cryst. Growth Des.* **2013**, *13* (2), 770–774. https://doi.org/10.1021/cg301493a

Darezereshki, E. One-step synthesis of hematite (α-Fe_2O_3) nano-particles by direct thermal-decomposition of maghemite. *Mater. Lett.* **2011**, *65* (4), 642–645. https://doi.org/10.1016/j.matlet.2010.11.030

Dézsi, I.; Coey, J. M. D. Magnetic and thermal properties of ϵ-Fe_2O_3. *Phys. Status Solidi*. **1973**, *15* (2), 681–685. https://doi.org/10.1002/pssa.2210150239

Ding, Y.; Morber, J. R.; Snyder, R. L.; Wang, Z. L. Nanowire Structural Evolution from Fe_3O_4 to ϵ-Fe_2O_3. *Adv. Funct. Mater.* **2007**, *17* (7), 1172–1178. https://doi.org/10.1002/adfm.200601024

Faria, D. L. A. de; Silva, S. V.; Oliveira, M. T. de. Raman microspectroscopy of some iron oxides and oxyhydroxides. *J. Raman Spectrosc.* **1997**, *28* (11), 873–878. https://doi.org/10.1002/(SICI)1097-4555(199711)28:11<873::AID-JRS177>3.0.CO;2-B

Forestier, H.; Guiot-Guillain, G. Ferromagnetic Variety of Fe_2O_3. *C. R. Acad. Sci.* **1934**, *199*, 720.

Gialanella, S.; Girardi, F.; Ischia, G.; Lonardelli, I.; Mattarelli, M.; Montagna, M. On the goethite to hematite phase transformation. *J. Therm. Anal. Calorim.* **2010**, *102*, 867–873. https://doi.org/10.1007/s10973-010-0756-2

Gich, M.; Roig, A.; Taboada, E.; Molins, E.; Bonafos, C.; Snoeck, E. Stabilization of metastable phases in spatially restricted fields: the case of the Fe_2O_3 polymorphs. *Faraday Discuss.* **2007**, *136*, 345–354. https://doi.org/10.1039/B616097B

Gich, M.; Gazquez, J.; Roig, A.; Crespi, A.; Fontcuberta, J.; Idrobo, J. C.; Pennycook, S. J.; Varela, M.; Skumryev, V.; Varela, M. Epitaxial stabilization of ε-Fe2O3 (00l) thin films on SrTiO3 (111). *Appl. Phys. Lett.* **2010**, *96*, 112508. https://doi.org/10.1063/1.3360217

Gonçalves, R. H.; Lima, B. H. R.; Leite, E. R. Magnetite Colloidal Nanocrystals: A Facile Pathway To Prepare Mesoporous Hematite Thin Films for Photoelectrochemical Water Splitting. *J. Am. Chem. Soc.* **2011**, *133* (15), 6012–6019. https://doi.org/10.1021/ja111454f

Gou, X.; Wang, G.; Park, J.; Liu, H.; Yang, J. Monodisperse hematite porous nanospheres: synthesis, characterization, and applications for gas sensors. *Nanotechnology*. **2008**, *19*, 125606. https://doi.org/10.1088/0957-4484/19/12/125606

Grasse, E. K.; Torcasio, M. H.; Smith, A. W. Teaching UV–Vis Spectroscopy with a 3D-Printable Smartphone Spectrophotometer. *J. Chem. Educ.* **2016**, *93* (1), 146–151. https://doi.org/10.1021/acs.jchemed.5b00654

Gratzel, M. Photoelectrochemical Cells. *Nature*. **2001**, *414*, 338–344. https://doi.org/10.1038/35104607

Gu, X.; Chen, L.; Ju, Z.; Xu, H.; Yang, J.; Qian, Y. Controlled Growth of Porous α-Fe2O3 Branches on β-MnO2 Nanorods for Excellent Performance in Lithium-Ion Batteries. *Adv. Funct. Mater.* **2013**, *23* (32), 4049–4056. https://doi.org/10.1002/adfm.201203779

Guettaï, N.; Amar, H. A. Photocatalytic Oxidation of Methyl Orange in Presence of Titanium Dioxide in Aqueous Suspension. Part II: Kinetics Study. *Desalination*. **2005**, *185* (1–3), 439–448. https://doi.org/10.1016/j.desal.2005.04.049

Huang, Y.; Ding, D.; Zhu, M.; Meng, W.; Huang, Y.; Geng, F.; Li, J.; Lin, J.; Tang, C.; Lei, Z.; Zhang, Z.; Zhi, C. Facile synthesis of α-Fe_2O_3 nanodisk with superior photocatalytic performance and mechanism insight. *Sci. Technol. Adv. Mater.* **2015**, *16* (1), 014801 (12pp). https://doi.org/10.1088/1468-6996/16/1/014801

Jin, J.; Ohkoshi, S.; Hashimoto, K. Giant Coercive Field of Nanometer- Sized Iron Oxide. *Adv. Mater.* **2004**, *16* (1), 48–51. https://doi.org/10.1002/adma.200305297

Keller, U. Recent Developments in Compact Ultrafast Lasers. *Nature.* **2003**, *424*, 831–838. https://doi.org/10.1038/nature01938

Kelm, K.; Mader, W. Synthesis and Structural Analysis of ϵ-Fe_2O_3. *Z. Anorg. Allg. Chem.* **2005**, *631* (12), 2383–1389. https://doi.org/10.1002/zaac.200500283

Kennedy, J. H.; Frese Junior, K. W. Photooxidation of Water at α - Fe_2O_3 Electrodes. *J. Electrochem. Soc.* **1978**, *125*, 709–714. https://doi.org/10.1149/1.2131532

Lassoued, A.; Lassoued, M. S.; Dkhil, B.; Gadri, A.; Ammar, S. Synthesis, structural, optical and morphological characterization of hematite through the precipitation method: Effect of varying the nature of the base. *J. Mol. Struct.* **2017**, *1141*, 99–106. https://doi.org/10.1016/j.molstruc.2017.03.077

Liong, M.; Lu, J.; Kovochich, M.; Xia, T.; Ruehm, S. G.; Nel, A. E.; Tamanoi, F.; Zink, J. I. Multifunctional Inorganic Nanoparticles for Imaging, Targeting, and Drug Delivery. *ACS Nano*. **2008**, *2* (5), 889–896. https://doi.org/10.1021/nn800072t

Liu, X. Q.; Tao, S. W.; Shen, Y. S. Preparation and characterization of nanocrystalline α-Fe2O3 by a sol-gel process. *Sens. Actuators B Chem*. **1997**, *40* (2–3), 161–165. https://doi.org/10.1016/s0925-4005(97)80256-0

López-Sánchez, J.; Serrano, A.; Del Campo, A.; Abuín, M.; Fuente, O. R. de la; Carmona, N. Sol–Gel Synthesis and Micro-Raman Characterization of ε-Fe2O3 Micro- and Nanoparticles. *Chem. Mater*. **2016**, *28* (2), 511–518. https://doi.org/10.1021/acs.chemmater.5b03566

Machala, L.; Tuček, J.; Zbořil, R. Polymorphous Transformations of Nanometric Iron(III) Oxide: A Review. *Chem. Mater.* **2011**, *23*, 3255–3272. https://doi.org/10.1021/cm200397g

Mandriota, G.; Corato, R.; Benedetti, M.; Castro, F. de; Fanizzi, F. P.; Rinaldi, R. Design and Application of Cisplatin-Loaded Magnetic Nanoparticle Clusters for Smart Chemotherapy. *ACS Appl. Mater. Interfaces.* **2019**, *11* (2), 1864–1875. https://doi.org/10.1021/acsami.8b18717

Marean, C. W.; Bar-Matthews, M.; Bernatchez, J.; Fisher, E.; Goldberg, P.; Herries, A. I. R.; Jacobs, Z.; Jerardino, A.; Karkanas, P.; Minichillo, T.; Nilssen, P. J.; Thompson, E.; Watts, I.; Williams, H. M. Early human use of marine resources and pigment in South Africa during the Middle Pleistocene. *Nature*. **2007**, *449*, 905–908. https://doi.org/10.1038/nature06204

McClean, R. G.; Schofield, M. A.; Kean, W. F.; Sommer, C. V.; Robertson, D. P.; Toth, D.; Gajdardziska-Josifovska, M. Botanical iron minerals: correlation between nanocrystal structure and modes of biological self-assembly. *Eur. J. Mineral.* **2001**, *13* (6), 1235–1242. https://doi.org/10.1127/0935-1221/2001/0013-1235

Pandey, B. K. Shahi, A. K.; Shah, J.; Kotnala, R. K.; Gopal, R. Optical and magnetic properties of Fe2O3 nanoparticles synthesized by laser ablation/fragmentation technique in different liquid media. *Appl. Surf. Sci.* **2014**, *289*, 462–471. https://doi.org/10.1016/j.apsusc.2013.11.009

Papynov, E. K.; Portnyagin, A. S.; Modin, E. B.; Mayorov, V. Y.; Shichalin, O. O.; Golikov, A. P.; Pechnikov, V. S.; Gridasova, E. A.; Tananaev, I. G.; Avramenko, V. A. A complex approach to assessing porous structure of structured ceramics obtained by SPS technique. *Mater. Charact.* **2018**, *145*, 294–302. https://doi.org/10.1016/j.matchar.2018.08.044

Petersen, N.; Schembera, N.; Schmidbauer, E.; Vali, H. Magnetization, mössbauer spectroscopy and structural studies of a ferrimagnetic Fe-Oxide formed by heating nontronite in air. *Phys. Chem. Miner*. **1987**, *14* (2), 118–121. https://doi.org/10.1007/BF00308215

Pinatti, I. M.; Gouveia, A. F.; Doñate-Buendía, C.; Mínguez-Vega, G.; Andrés, J.; Longo, E. Femtosecond-Laser-Irradiation-Induced Structural Organization and Crystallinity of Bi2WO6. *Sci. Rep.* **2020**, *10*, 4613. https://doi.org/10.1038/s41598-020-61524-y

Pottker, W. E.; Ono, R.; Cobos, M. A.; Hernando, A.; Araujo, J. F. D. F.D; Bruno, A. C. O.; Lourenço, S. A.; Longo, E.; La Porta, F. A. Influence of order-disorder effects on the magnetic and optical properties of NiFe2O4 nanoparticles. *Ceram. Int.* **2018**, *44* (14), 17290–17297. https://doi.org/10.1016/j.ceramint.2018.06.190

Rietveld, H. M. A profile refinement method for nuclear and magnetic structures. *J. Appl. Crystallogr*. **1969**, *2*, 65–71. https://doi.org/10.1107/S0021889869006558

Sakurai, S.; Jin, J.; Hashimoto, K.; Ohkoshi, S. Reorientation Phenomenon in a Magnetic Phase of ε-Fe2O3 Nanocrystal. *J. Phys. Soc. Japan*. **2005**, *74* (7), 1946–1949. https://doi.org/10.1143/JPSJ.74.1946

Sakurai, S.; Namai, A.; Hashimoto, K.; Ohkoshi, S. First Observation of Phase Transformation of All Four Fe2O3 Phases (γ → ε → β → α-Phase). *J. Am. Chem. Soc.* **2009**, *131* (51), 18299–18303. https://doi.org/10.1021/ja9046069

Sans, J. A.; Monteseguro, V.; Garbarino, G.; Gich, M.; Cerantola, V.; Cuartero, V.; Monte, M.; Irifune, T.; Muñoz, A.; Popescu, C. Stability and nature of the volume collapse of ε-Fe2O3 under extreme conditions. *Nat. Commun*. **2018**, *9*, 4554. https://doi.org/10.1038/s41467-018-06966-9

Sarma, S. K.; Mohan, R.; Shukla, A. Structural, opto-electronic and photoelectrochemical properties of tin doped hematite nanoparticles for water splitting. *Mater. Sci. Semicond. Process.* **2020**, *108*, 104873. https://doi.org/10.1016/j.mssp.2019.104873

Schneider, C. A.; Rasband, W. S.; Eliceiri, K. W. NIH Image to ImageJ: 25 years of image analysis. *Nat. Methods.* **2012**, *9*, 671–675. https://doi.org/10.1038/nmeth.2089

Schrader, R.; Büttner, G. Eine neue Eisen(III)-oxidphase: ϵ-Fe_2O_3. *Z. Anorg. Allg. Chem.* **1963**, *320* (5–6), 220–234. https://doi.org/10.1002/zaac.19633200503

Sepúlveda, M.; Gallardo, F.; Ballester, B.; Cabello, G.; Vidal, E. El Condor mine: Prehispanic production and consumption of hematite pigments in the Atacama Desert, northern Chile. *J. Anthropol. Archaeol*. **2019**, *53*, 325–341. https://doi.org/10.1016/j.jaa.2018.04.001

Shabalina, I. G.; Porebskia, P. J.; Minor, W. Refining the macromolecular model – achieving the best agreement with the data from X-ray diffraction experiment. *Crystallogr. Rev.* **2018**, *24* (4), 236–262. https://doi.org/10.1080/0889311X.2018.1521805

Shanenkov, I.; Sivkov, A.; Ivashutenko, A.; Medvedeva, T.; Shchetinin, I. High-energy plasma dynamic synthesis of multiphase iron oxides containing Fe_3O_4 and ε-Fe_2O_3 with possibility of controlling their phase composition. *J. Alloys*

Eclética Química Journal, vol. 47, special issue 1, 2022, 105-119
ISSN: 1678-4618
DOI: 10.26850/1678-4618eqj.v47.1SI.2022.p105-119

Compd. **2019**, *774*, 637–645. https://doi.org/10.1016/j.jallcom.2018.10.019

Sharma, P.; Kaur, H.; Sharma, M.; Sahore, V. A review on applicability of naturally available adsorbents for the removal of hazardous dyes from aqueous waste. *Environ. Monit. Assess.* **2011**, *183*, 151–195. https://doi.org/10.1007/s10661-011-1914-0

Sheng, C.; Mat Yunus, W. Study of Photobleaching Mechanism in Methylene Blue Sensitized Gelatin Using a Single Beam UV-Vis. Fibre Optics Spectrophotometer. *Pertanika J. Sci. Technol.* **2005**, *13* (1), 23–30.

Sivula, K.; Zboril, R.; Le Formal, F.; Robert, R.; Weidenkaff, A.; Tucek, J.; Frydrych, J.; Grätzel, M. Photoelectrochemical Water Splitting with Mesoporous Hematite Prepared by a Solution-Based Colloidal Approach. *J. Am. Chem. Soc.* **2010**, *132* (21), 7436–7444. https://doi.org/10.1021/ja101564f

Sivula, K.; Le Formal, F.; Grätzel, M. Solar Water Splitting: Progress Using Hematite (α-Fe_2O_3) Photoelectrodes. *ChemSusChem.* **2011**, *4* (4), 432–449. https://doi.org/10.1002/cssc.201000416

Sugioka, K.; Cheng, Y. Ultrafast lasers—reliable tools for advanced materials processing. *Light Sci. Appl.* **2014**, *3*, e149. https://doi.org/10.1038/lsa.2014.30

Tamirat, A. G.; Rick, J.; Dubale, A. A.; Su, W.-N.; Hwang, B.-J. Using hematite for photoelectrochemical water splitting: a review of current progress and challenges. *Nanoscale Horiz.* **2016**, *1* (4), 243–267. https://doi.org/10.1039/C5NH00098J

Trench, A. B.; Machado, T. R.; Gouveia, A. F.; Assis, M.; Trindade, L. G. da; Santos, C.; Perrin, A.; Perrin, C.; Oliva, M.; Andrés, J.; Longo, E. Connecting structural, optical, and electronic properties and photocatalytic activity of Ag_3PO_4:Mo complemented by DFT calculations. *Appl. Catal. B.* **2018**, *238*, 198–211. https://doi.org/10.1016/j.apcatb.2018.07.019

Trindade, L. G. da; Hata, G. Y.; Souza, J. C.; Soares, M. R. S.; Leite, E. R.; Pereira, E. C.; Longo, E.; Mazzo, T. M. Preparation and characterization of hematite nanoparticles-decorated zinc oxide particles (ZnO/Fe_2O_3) as photoelectrodes for solar cell applications. *J. Mater. Sci.* **2020**, *55*, 2923–2936. https://doi.org/10.1007/s10853-019-04135-x

Tronc, E.; Chanéac, C.; Jolivet, J. P. Structural and Magnetic Characterization ofε-Fe_2O_3. J. *Solid State Chem.* **1998**, *139* (1), 93–104. https://doi.org/10.1006/jssc.1998.7817

Tuček, J.; Machala, L.; Ono, S.; Namai, A.; Yoshikiyo, M.; Imoto, K.; Tokoro, H.; Ohkoshi, S.; Zbořil, R. Zeta-Fe_2O_3 – A new stable polymorph in iron(III) oxide family. *Sci. Rep.* **2015**, *5*, 1–11. https://doi.org/10.1038/srep15091

Vadivel, S.; Vanitha, M.; Muthukrishnaraj, A.; Balasubramanian, N. Graphene oxide–BiOBr composite material as highly efficient photocatalyst for degradation of methylene blue and rhodamine-B dyes. *J. Water Process. Eng.* **2014**, *1*, 17–26. https://doi.org/10.1016/j.jwpe.2014.02.003

Von Dreele, R. B.; Larson, A. C. *General Structure Analysis System (GSAS)*. Los Alamos National Lab; 1994, p. 86–748. URL. https://permalink.lanl.gov/object/tr?what=info:lanl-repo/lareport/LA-UR-86-0748_REV (accessed 2022-02-04).

Vu, X. H.; Phuoc, L. H.; Dien, N. D.; Pham, T. T. H.; Thanh, L. D. Photocatalytic Degradation of Methylene Blue (MB) over α-Fe_2O_3 Nanospindles Prepared by a Hydrothermal Route. *J. Electron. Mater.* **2019**, *48*, 2978–2985. https://doi.org/10.1007/s11664-019-07056-2

Wang, T. H.; Lin, C.-A.; Xu, S.; Wang, C.-F.; Chen, C.-W.; Dong, C.-D.; Huang, C. P. Toward concurrent organics removal and potential hydrogen production in wastewater treatment: Photoelectrochemical decolorization of methylene blue over hematite electrode in the presence of Mn(II). *Appl. Catal. B.* **2019**, *244*, 140–149. https://doi.org/10.1016/j.apcatb.2018.11.048

Wheeler, D. A.; Wang, G.; Ling, Y.; Li, Y.; Zhang, J. Z. Nanostructured hematite: synthesis, characterization, charge carrier dynamics, and photoelectrochemical properties. *Energy Environ. Sci.* **2012**, *5*, 6682–6702. https://doi.org/10.1039/C2EE00001F

Wood, D. L.; Tauc, J. Weak Absorption Tails in Amorphous Semiconductors. *Phys. Rev. B.* **1972**, *5* (8), 3144–3151. https://doi.org/10.1103/PhysRevB.5.3144

Zboril, R.; Mashlan, M.; Petridis, D. Iron(III) Oxides from Thermal Processes Synthesis, Structural and Magnetic Properties, Mössbauer Spectroscopy Characterization, and Applications. *Chem. Mater.* **2002**, *14* (3), 969–982. https://doi.org/10.1021/cm0111074

Zhao, W.; Ma, W.; Chen, C.; Zhao, J.; Shuai, Z. Efficient Degradation of Toxic Organic Pollutants with Ni_2O_3/TiO_2-xBx under Visible Irradiation. J. Am. Chem. Soc. **2004**, 126 (15), 4782–4783. https://doi.org/10.1021/ja0396753

Eclética Química Journal, vol. 47, special issue 1, 2022, 105-119
ISSN: 1678-4618
DOI: 10.26850/1678-4618eqj.v47.1SI.2022.p105-119